

Time-dependent viscoplastic fluid flow simulations in two and three dimensions

Knut Sverdrup^a, Nikolaos Nikiforakis^a, Ann Almgren^b

^aCentre for Scientific Computing, Cavendish Laboratory, University of Cambridge, CB3 0HE, UK

^bCenter for Computational Sciences and Engineering, Lawrence Berkeley National Lab, CA 94720, USA

Abstract

We present the extension of an efficient and highly parallelisable framework for incompressible fluid flow simulations to viscoplastic fluids. The system is governed by the incompressible Navier-Stokes equations and a generalised Newtonian constitutive equation. In order to simulate a wide range of viscoplastic fluids, we employ the Herschel-Bulkley model for yield-stress fluids with nonlinear stress-strain dependency above the yield limit. We utilise Papanastasiou regularisation in our algorithm to deal with the singularity in apparent viscosity. The resulting system of partial differential equations is solved using the IAMR code (Incompressible Adaptive Mesh Refinement), which uses second-order Godunov methodology for the advective terms and semi-implicit diffusion in the context of an approximate projection method. By augmenting the IAMR code with the ability to simulate regularised Herschel-Bulkley fluids, we obtain efficient numerical software for viscoplastic flow which can be used to investigate systems previously considered too expensive computationally. We validate results from simulations using this new capability against previously published data for Bingham plastics and power-law fluids in the two-dimensional lid-driven cavity. In doing so, we expand the range of Bingham and Reynolds numbers which have been considered in the benchmark tests. Moreover, extensions to time-dependent flow of Herschel-Bulkley fluids and three spatial dimensions offer new insights into the flow of viscoplastic fluids in this test case.

Keywords: Viscoplasticity, Herschel-Bulkley fluids, Papanastasiou regularisation, lid-driven cavity, high performance computing

1. Introduction

Viscoplastic fluids are non-Newtonian fluids which are characterised by a minimum induced stress necessary for flow to occur. For this reason they are also commonly referred to as yield-stress fluids. When the imposed stress does not exceed the threshold value, the material is modelled as a rigid solid. In regions where the yield stress is exceeded, however, the material flows like a fluid. The ability of the material to support a stress under certain circumstances gives rise to phenomena such as non-flat surfaces at rest under gravity and the coexistence of yielded (flowing) and unyielded (rigid) regions within the fluid. The former can be demonstrated by distorting the surface of mayonnaise in a jar: gravity alone is not strong enough to surpass the yield stress, and the surface remains in its distorted state. In addition to being fundamentally interesting from the perspectives of rheology, fluid mechanics and mathematical modelling, yield stress fluids occur naturally and are paramount to the success of animals such as mudskippers^[1] and snails^[2]. Their importance in industries ranging from medicine^[3–6] to oil and gas exploration^[7–9] has led to extensive research contributions in the field.

Just as for Newtonian fluids, the pursuit of knowledge about viscoplastic fluids has relied heavily on computational methods in the last fifty years. Compared to the

Newtonian case, however, the numerical simulations are much more demanding in terms of processing time. This is largely due to the existence of a yield stress, since this results in a singularity at zero strain rate for the apparent viscosity of the fluid. Traditional methods for computing the solution are rendered useless for this case, since infinite viscosities cannot be represented in the unyielded regions. There are now two main branches of algorithms designed to deal with this problem. The first utilises mathematical regularisation to approximate the viscosity function in the low-strain limit. In doing so, the rigid body approximation is effectively replaced by a fluid with very high viscosity in the unyielded regions. A regularisation parameter controls how close this approximation is to the idealised viscoplastic case. On the other hand, the problem can be reformulated in the framework of non-smooth optimisation theory, and solved using augmented Lagrangians. Such methods can solve the unregularised problem without introducing any approximations, but require more computational resources to find the solution.

The regularisation approach was first explored by Bercovier and Engelman in 1980^[10], who utilised a simple yet efficient work-around by adding a small constant to the computed strain-rate, so that even in the zero-strain limit the viscosity would remain finite. An alternative method proposed by Tanner and Milthorpe a few years later was the bi-viscosity model^[11], in which the viscoplastic fluid

Email address: ksk38@cam.ac.uk (Knut Sverdrup)

is characterised by a separate, large viscosity when the strain-rate is below a given threshold. An exponential regularisation factor was then introduced by Papanastasiou in 1987^[12], and this method of regularisation is still widely used in modern codes which deal with viscoplasticity through regularisation. Important investigations based on Papanastasiou regularisation include those of Mitsoulis et al.^[13–16] and Syrakos et al.^[17–19].

Augmented Lagrangian methods were first applied to the viscoplastic flow problem in 1983 by Fortin and Glowinski^[20], but the variational formulation on which it relies was derived by Duvaut and Lions in 1976, who studied existence, uniqueness and regularity of solutions to the problem^[21]. The augmented Lagrangian algorithm itself is due to Hestenes (1969)^[22]. Although the simulation of viscoplastic flow using this optimisation technique constitutes an important milestone in the history of its numerical treatments, the regularisation approach was much more popular due to the large discrepancy in computational resource requirements. Advances in convex optimisation over the next few decades led to the work of Saramito and Roquet^[23], where significant improvements were achieved in terms of convergence rates, and hence, computational efficiency. Other contributions^[24] further confirmed the potential, and in recent years state-of-the-art algorithms are actively being developed, notably by Treskatis^[25] and Saramito^[26]. Due to the ability to solve the unregularised viscoplasticity problem, these methods have become increasingly popular since algorithmic advances have led to significant speed-up of their runtime. It is important to note, however, that these methods are still more costly than regularised approaches, so although they allow computation of exact locations of yield surfaces, they are unnecessarily expensive when this is less important, and a general understanding of the flow field is desirable. An example is within cement displacement complexities for engineering purposes^[27], where the desirable insight is pressure distributions and the cement displacement efficiency.

Numerical treatment of viscoplastic flow problems has significantly improved over the last decades. Researchers interested in analysing such flows are, however, still limited by the computational cost associated with their solution. Notably, most research published in the field considers only two spatial dimensions and only steady-state solutions. Our contribution addresses this by providing an open-source code allowing simulation of the temporal evolution of Herschel-Bulkley fluids in three spatial dimensions. In order to achieve this, we begin with the IAMR^[28] code, that uses a second-order accurate, approximate projection method to solve the incompressible Navier-Stokes equations. The code is built on the AMReX software framework for developing massively parallel block-structured AMR applications. We have implemented the Papanastasiou regularised Herschel-Bulkley model for the apparent viscosity function in IAMR so that it can be used to simulate generalised Newtonian fluids. As such, we are able to take advantage of modern supercomputer

architectures in our simulation of viscoplastic fluids. For the first time, results are presented for the transient, three-dimensional lid-driven cavity problem for viscoplastic fluids. Notably, the evolution of the three-dimensional yield surface from rest to steady-state is tracked, before the lid velocity is set to zero, allowing cessation of the viscoplastic fluid.

For further reading on developments in viscoplastic fluids, we refer the reader to the review papers by Barnes^[29] and Balmforth et al.^[30]. Additionally, two excellent review papers on advances in numerical simulations of these fluids appeared in a recent special edition of *Rheologica Acta*^[16,31]. In section 2, we will introduce the governing partial differential equations and discuss relevant fluid rheologies. Section 3 is devoted to the numerical algorithm employed to simulate the fluid flow, including the regularisation strategy. Thorough validation is performed in section 4, before we evaluate the code for Herschel-Bulkley fluids and three dimensions in section 5. Section 6 concludes the article.

2. Mathematical formulation

Our domain $\Omega \subset \mathbb{R}^d$ is either in two or three dimensions, i.e. $d \in \{2, 3\}$. For rank-1 tensors, we prescribe the Frobenius inner product:

$$\mathbf{A} : \mathbf{B} = \text{tr}(\mathbf{A}\mathbf{B}^\top) = \sum_{i=1}^d \sum_{j=1}^d A_{ij}B_{ij} \quad \forall (\mathbf{A}, \mathbf{B}) \in \mathbb{R}^{d \times d}. \quad (1)$$

Consequently, the induced norms of these quantities are given by¹

$$|\mathbf{A}| = \sqrt{\text{tr}(\mathbf{A}\mathbf{A}^\top)}. \quad (2)$$

We take the gradient of a vector \mathbf{u} as the tensor with components $(\nabla \mathbf{u})_{ij} = \partial u_j / \partial x_i$, and the symmetric part of this gradient is given by $\mathcal{D}\mathbf{u} = \frac{1}{2}(\nabla + \nabla^\top)\mathbf{u}$. The divergence of a tensor field is defined such that $(\nabla \cdot \mathbf{A})_j = \sum_{i=1}^d \partial A_{ij} / \partial x_i$. Variables are functions of position $\mathbf{x} \in \Omega$ and time $t \geq 0$.

2.1. Governing partial differential equations

We denote by $\rho \in \mathbb{R}$ the material density. The velocity field is introduced as $\mathbf{u}(\mathbf{x}, t) \in \mathbb{R}^d$, with components u , v and w . The Cauchy stress tensor $\boldsymbol{\sigma}$ is defined as the sum of isotropic and deviatoric parts, $\boldsymbol{\sigma} = -p\mathbf{I} + \boldsymbol{\tau}$. Here, the pressure $p(\mathbf{x}, t) \in \mathbb{R}$ is multiplied by the identity tensor, while the deviatoric part of the stress tensor is denoted $\boldsymbol{\tau}(\mathbf{x}, t) \in \mathbb{R}_{\text{sym}}^{d \times d}$. The fluid motion is then governed by

¹Note that many authors on viscoplasticity use a tensor norm which differs from this by a factor $\sqrt{2}$, since doing so slightly simplifies the analytical solution of simple shear flows.

the incompressible Navier-Stokes equations, comprised of mass conservation and momentum balance:

$$\nabla \cdot \mathbf{u} = 0, \quad (3a)$$

$$\frac{\partial \mathbf{u}}{\partial t} + \mathbf{u} \cdot \nabla \mathbf{u} = \frac{1}{\rho} (-\nabla p + \nabla \cdot \boldsymbol{\tau} + \mathbf{f}). \quad (3b)$$

Here, we have introduced \mathbf{f} to describe external body forces such as gravity acting on the fluid. Note that the mass conservation equation is simplified to (3a) due to incompressibility, i.e. constant density within a fluid parcel.

2.2. Rheology

We shall in the following restrict ourselves to relatively simple equations of state on the form $\boldsymbol{\tau} = \boldsymbol{\tau}(\dot{\boldsymbol{\gamma}})$, where the stress response is solely dependent on the rate-of-strain tensor $\dot{\boldsymbol{\gamma}} = \mathcal{D}\mathbf{u} \in \mathbb{R}_{\text{sym}}^{n \times n}$. Although the Herschel-Bulkley model captures all aspects of the fluids considered, references for validation are only available for power-law and Bingham fluids. For this reason, we introduce these simpler rheological models first, and illustrate how they can be combined.

Newtonian flow is characterised by a dynamic coefficient of viscosity $\mu > 0$ which is independent of the shear, yielding a linear relationship between rate-of-strain and stress in the rheological equation:

$$\boldsymbol{\tau} = 2\mu\dot{\boldsymbol{\gamma}}. \quad (4)$$

For fluids where the dependency of the stress on the rate-of-strain tensor is nonlinear, the apparent viscosity is a useful concept when considering rheological responses to shear. It is a generalisation of the constant viscosity for Newtonian flow, where we allow the viscosity to be a function of the magnitude of the rate-of-strain tensor. Denoting the apparent viscosity by η , we thus have

$$\eta = \frac{|\boldsymbol{\tau}|}{2|\dot{\boldsymbol{\gamma}}|}. \quad (5)$$

Many fluids are accurately modelled by a non-Newtonian behaviour that captures shear-dependency through a smooth increase or decrease in apparent viscosity. Such fluids include pseudoplastics (shear-thinning, $\partial\eta/\partial|\dot{\boldsymbol{\gamma}}| < 0$) and dilatants (shear-thickening, $\partial\eta/\partial|\dot{\boldsymbol{\gamma}}| > 0$). A model which captures this behaviour is the power-law fluid, with rheological equation

$$\boldsymbol{\tau} = 2^{\frac{n+1}{2}} \mu |\dot{\boldsymbol{\gamma}}|^{n-1} \dot{\boldsymbol{\gamma}}, \quad (6)$$

and apparent viscosity

$$\eta = 2^{\frac{n-1}{2}} \mu |\dot{\boldsymbol{\gamma}}|^{n-1}. \quad (7)$$

A specific power-law fluid is characterised by its flow behaviour index $n > 0$ (and μ , which is usually referred to as the consistency for power-law fluids, and has units Pa s^n). From (6) it is immediately clear that the Newtonian case

with $n = 1$ separates pseudoplastics ($n < 1$) from dilatants ($n > 1$).

Viscoplastic fluids have a stress threshold $\tau_0 > 0$ (the yield stress), below which they do not flow. We note that it is possible to describe elastic deformation for materials which do not flow, but we shall be considering constitutive equations which assume a rigid body approximation, i.e. zero strain rate below the yield stress.

The simplest type of viscoplastic fluid is the Bingham fluid^[32,33], characterised by zero strain rate below the yield stress. In the yielded region, however, the stress depends linearly on the rate-of-strain magnitude, just like a Newtonian fluid. The stress-strain curve thus intercepts the $|\boldsymbol{\tau}|$ -axis at the point $(0, \tau_0)$. As such, the Bingham fluid is a generalised Newtonian, with rheological equation

$$\begin{cases} \dot{\boldsymbol{\gamma}} = 0 & \text{if } |\boldsymbol{\tau}| \leq \tau_0 \\ \boldsymbol{\tau} = 2\mu\dot{\boldsymbol{\gamma}} + \frac{\tau_0}{|\dot{\boldsymbol{\gamma}}|}\dot{\boldsymbol{\gamma}} & \text{if } |\boldsymbol{\tau}| > \tau_0 \end{cases} \quad (8)$$

and apparent viscosity

$$\eta = \mu + \frac{\tau_0}{2|\dot{\boldsymbol{\gamma}}|}. \quad (9)$$

For Bingham plastics, we refer to μ as the plastic viscosity, and note that η has a singularity for $\dot{\boldsymbol{\gamma}} = 0$, as expected.

In many applications, it is desirable to capture both the yield stress of viscoplastic fluids and the power-law dependency occurring once the fluid starts flowing. A widely used rheological model for such fluids is due to Herschel and Bulkley^[34]. The Herschel-Bulkley fluid facilitates a very general description of non-Newtonian fluids, as it is a yield stress fluid with a nonlinear stress-strain dependency in the yielded region. As such, it can be thought of as a hybrid between Bingham plastics and power law fluids. The constitutive equation is

$$\begin{cases} \dot{\boldsymbol{\gamma}} = 0 & \text{if } |\boldsymbol{\tau}| \leq \tau_0 \\ \boldsymbol{\tau} = 2^{\frac{n+1}{2}} \mu |\dot{\boldsymbol{\gamma}}|^{n-1} \dot{\boldsymbol{\gamma}} + \frac{\tau_0}{|\dot{\boldsymbol{\gamma}}|}\dot{\boldsymbol{\gamma}} & \text{if } |\boldsymbol{\tau}| > \tau_0 \end{cases}, \quad (10)$$

while the apparent viscosity is

$$\eta = 2^{\frac{n-1}{2}} \mu |\dot{\boldsymbol{\gamma}}|^{n-1} + \frac{\tau_0}{2|\dot{\boldsymbol{\gamma}}|}. \quad (11)$$

Bingham plastics are a special case of Herschel-Bulkley fluids in exactly the same manner as Newtonian fluids follow a specific power-law constitutive equation. Plots of the rheological characteristic for Herschel-Bulkley fluids are shown in figure 1, for various values of n . Note that the Bingham fluid is recovered for $n = 1$.

3. Numerical algorithm

3.1. Incompressible Navier-Stokes solver

An approximate projection method for solving the variable density incompressible Navier-Stokes equations on an adaptive mesh hierarchy has been implemented in the IAMR

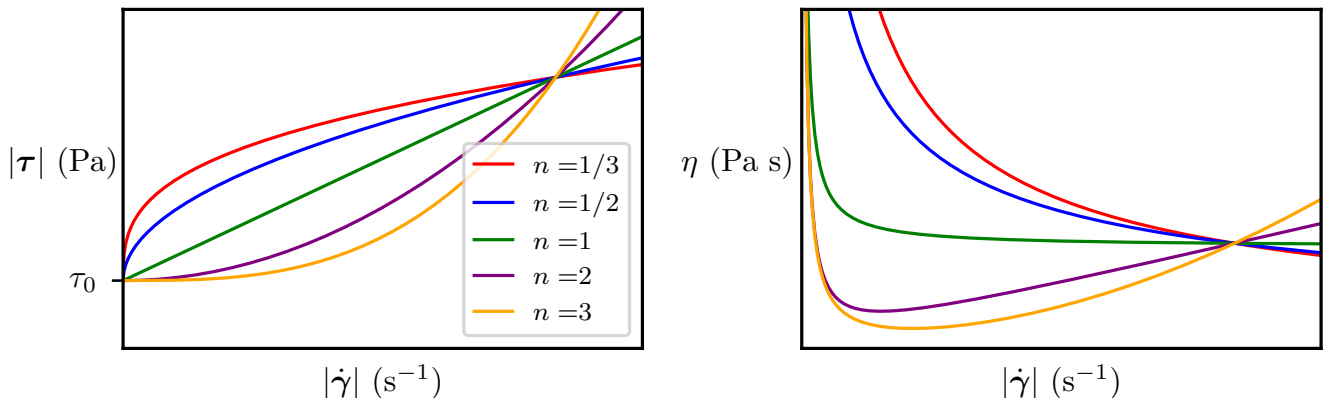


Figure 1: Herschel-Bulkley fluid: stress magnitude (left) and apparent viscosity (right) as functions of the magnitude of the rate-of-strain tensor $\dot{\gamma}$.

code. The algorithm was described for the constant viscosity case by Almgren et al. [28], with extensions to low Mach number reacting flows with temperature-dependent viscosity provided by Pember et al. [35] and Day and Bell [36], among others. In addition to solving the Navier-Stokes equations for velocity and pressure, the IAMR code allows for the (conservative or passive) advection of any number of scalar quantities. The implementation is such that the code can be run on architectures from single-core laptops through massively parallel supercomputers.

In the approximate projection method as implemented in IAMR, an advection-diffusion step is used to advance the velocity in time; the solution is then (approximately) projected onto the space of divergence-free fields. In the advection-diffusion step, Eq. (3b), is discretized in time to construct a new-time provisional velocity field, \mathbf{u}^* , without enforcing (3a). i.e. we define \mathbf{u}^* using

$$\frac{\mathbf{u}^* - \mathbf{u}^n}{\Delta t} = -[\mathbf{u}^{\text{MAC}} \cdot \nabla \tilde{\mathbf{u}}]^{n+1/2} + \frac{1}{\rho} \left(-\mathbf{G}p^{n-1/2} + \frac{1}{2} (\nabla \cdot \boldsymbol{\tau}(\mathbf{u}^n) + \nabla \cdot \boldsymbol{\tau}(\mathbf{u}^*)) + \mathbf{f}^n \right), \quad (12)$$

where $\mathbf{G}p^{n-1/2}$ is a lagged approximation to the pressure gradient ∇p and the density ρ is a constant².

The time-centered advective update term, $[\mathbf{u}^{\text{MAC}} \cdot \nabla \tilde{\mathbf{u}}]^{n+1/2}$ is constructed using an unsplit second-order accurate upwind scheme. All velocity components are predicted from cell centers at time t^n to faces at time $t^{n+1/2}$ using Taylor series approximations to define $\tilde{\mathbf{u}}$. The face-centered normal velocities are then projected to be divergence-free to define \mathbf{u}^{MAC} ; these velocities are used to advect scalars as well. The explicit viscous term, $\boldsymbol{\tau}(\mathbf{u}^n)$, is evaluated us-

ing only the velocity components at time t^n , i.e. we define $\dot{\boldsymbol{\gamma}}^n = \dot{\boldsymbol{\gamma}}(\mathbf{u}^n)$, $\eta^n = \eta(\dot{\boldsymbol{\gamma}}^n)$ and write $\boldsymbol{\tau}(\mathbf{u}^n) = 2\eta^n \dot{\boldsymbol{\gamma}}^n$.

We solve for \mathbf{u}^* with the same η^n , i.e.

$$\left(\mathbf{u}^* - \frac{\Delta t}{\rho} \nabla \cdot (\eta^n \dot{\boldsymbol{\gamma}}^*) \right) = \mathbf{u}^n - \Delta t [\mathbf{u}^{\text{MAC}} \cdot \nabla \tilde{\mathbf{u}}]^{n+1/2} + \frac{\Delta t}{\rho} \left(-\mathbf{G}p^{n-1/2} + \nabla \cdot (\eta^n \boldsymbol{\gamma}^n) + \mathbf{f}^n \right). \quad (13)$$

Note that all velocity components are solved for simultaneously.

The final part of the algorithm is the projection step and subsequent pressure update. The velocity field \mathbf{u}^* does not in general satisfy the divergence constraint as given by (3a). We solve

$$L_\rho \phi = D \left(\frac{1}{\Delta t} \mathbf{u}^* + \frac{1}{\rho} \mathbf{G}p^{n-1/2} \right) \quad (14)$$

where D is a discrete divergence and \mathbf{G} a discrete gradient. L_ρ is a second-order accurate approximation to $\nabla \cdot \frac{1}{\rho} \nabla$. The new-time velocity is then defined by

$$\mathbf{u}^{n+1} = \mathbf{u}^* - \Delta t \frac{1}{\rho} \mathbf{G} \phi \quad (15)$$

and the updated pressure by

$$p^{n+1/2} = \phi. \quad (16)$$

For further detail on the algorithm, see the original paper by Almgren et al. [28]

3.2. Regularisation of viscosity

Equation (10) does not present any problems for unyielded regions ($\dot{\boldsymbol{\gamma}} > 0$), but the apparent viscosity has a singularity when the strain rate approaches zero (and $|\boldsymbol{\tau}| \rightarrow \tau_0$). Computational schemes such as those implemented in IAMR cannot be used in the presence of such

²IAMR is designed for more general flows with variable density; however for the flows considered in this paper the density is constant in space and time.

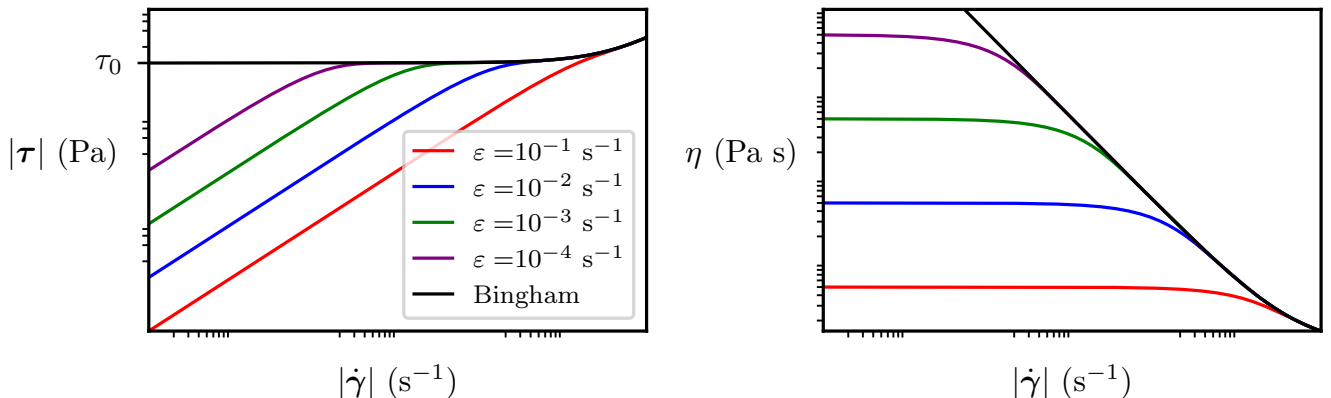


Figure 2: Papanastasiou regularisation for the Bingham model: stress magnitude (left) and apparent viscosity (right) as functions of the magnitude of the rate-of-strain tensor $|\dot{\gamma}|$. For decreasing ϵ , we recover a closer approximation to the actual Bingham model. Note that logarithmic axes are employed in order to highlight the behaviour in the low-strain limit.

singularities. Regularisation deals with the problem by replacing the ill-behaved apparent viscosity with a function that approximates the rheological behaviour, but which stays bounded for arbitrarily small $\dot{\gamma}$. This is done by introducing an additional parameter ϵ to the apparent viscosity, which describes how big the effect of the regularisation is. A large value of ϵ allows for inexpensive computations even near unyielded flow, while the limit $\epsilon \rightarrow 0$ recovers the unregularised description. Note that one must be careful to choose a small enough value for ϵ , in addition to fine enough mesh resolutions and convergence criterion. Otherwise, the mathematical approximation will not hold.

We employ the popular Papanastasiou regularisation^[12], which utilises an exponential relaxation according to

$$\frac{1}{|\dot{\gamma}|} \rightarrow \frac{1 - e^{-|\dot{\gamma}|/\epsilon}}{|\dot{\gamma}|}. \quad (17)$$

This is a good approximation for $|\dot{\gamma}|/\epsilon \gg 1$, while in the small strain limit we have

$$\lim_{|\dot{\gamma}| \rightarrow 0} \frac{1 - e^{-|\dot{\gamma}|/\epsilon}}{|\dot{\gamma}|} = \lim_{|\dot{\gamma}| \rightarrow 0} \frac{1}{|\dot{\gamma}|} \left(1 - \sum_{k=0}^{\infty} \frac{(-|\dot{\gamma}|/\epsilon)^k}{k!} \right) = \frac{1}{\epsilon}, \quad (18)$$

so that it always remains bounded, and recovers the unregularised model in the limit $\epsilon \rightarrow 0$. Combination of (17) with the apparent viscosity as given in (10), gives the regularised viscosity as

$$\eta = \left(2^{\frac{n-1}{2}} \mu |\dot{\gamma}|^{n-1} + \frac{\tau_0}{2|\dot{\gamma}|} \right) \left(1 - e^{-|\dot{\gamma}|/\epsilon} \right). \quad (19)$$

The effect of varying the regularisation parameter ϵ is shown in figure 2. In the Papanastasiou-regularised Herschel-Bulkley model, the singularity in apparent viscosity is replaced by the limiting value

$$\lim_{|\dot{\gamma}| \rightarrow 0} \eta = \frac{\tau_0}{2\epsilon}. \quad (20)$$

3.3. Parallel Implementation

AMReX is a mature, open source software framework for building massively parallel block-structured adaptive mesh refinement (AMR) applications. AMReX contains extensive software support for explicit and implicit grid-based operations; multigrid solvers, including those for tensor systems, are included for cell-based and node-based data. AMReX uses a hybrid MPI/OpenMP approach for parallelization; in this model individual grids are distributed to MPI ranks, and OpenMP is used to thread over logical tiles within the grids. Applications based on AMReX have demonstrated excellent strong and weak scaling up to hundreds of thousands of cores.

4. Validation

In order to validate our code, we consider the two-dimensional lid driven cavity test case. It is a historically significant and widely used benchmark problem for viscous flow simulations, and consequently a large amount of reference results exist in the literature. Our domain is a square of side length \mathcal{L} , i.e. $\Omega = [0, \mathcal{L}]^2$, and is filled with a fluid of constant density. Initially, the system is at rest. All walls except the top (“the lid”) are held fixed, so that the boundary conditions on these walls are $\mathbf{u} = (0, 0)$. At time $t = 0$, the lid is instantaneously prescribed the tangential velocity \mathcal{U} , so that the relevant boundary condition for $t > 0$ is $\mathbf{u} = (\mathcal{U}, 0)$. Without any other external forces ($\mathbf{f} = 0$), this drives a recirculating flow in the cavity, which reaches a steady-state solution for non-turbulent regimes.

In order to obtain a dimensionless form of (3), we let $\hat{\mathbf{x}} = \mathbf{x}/\mathcal{L}$, $\hat{\mathbf{u}} = \mathbf{u}/\mathcal{U}$ and $\hat{t} = t/(\mathcal{L}/\mathcal{U})$. Additionally, we

take \mathcal{U}/\mathcal{L} as a characteristic strain-rate, and let

$$\hat{\boldsymbol{\gamma}} = \frac{\dot{\boldsymbol{\gamma}}}{\frac{\mathcal{U}}{\mathcal{L}}}, \quad \hat{\eta} = \frac{\eta}{2^{\frac{n-1}{2}} \mu \left(\frac{\mathcal{U}}{\mathcal{L}}\right)^{n-1}}, \quad (21)$$

$$\hat{p} = \frac{p}{2^{\frac{n-1}{2}} \mu \left(\frac{\mathcal{U}}{\mathcal{L}}\right)^n}, \quad \hat{\boldsymbol{\tau}} = \frac{\boldsymbol{\tau}}{2^{\frac{n-1}{2}} \mu \left(\frac{\mathcal{U}}{\mathcal{L}}\right)^n}. \quad (22)$$

By substituting these dimensionless variables into (3), we find that the governing equations in dimensionless form are

$$\frac{\partial \hat{\mathbf{u}}}{\partial \hat{t}} + \hat{\mathbf{u}} \cdot \hat{\nabla} \hat{\mathbf{u}} = \frac{1}{Re} \left(-\hat{\nabla} \hat{p} + \hat{\nabla} \cdot \hat{\boldsymbol{\tau}} \right), \quad (23a)$$

$$\hat{\nabla} \cdot \hat{\mathbf{u}} = 0, \quad (23b)$$

$$\hat{\eta} = \left(|\hat{\boldsymbol{\gamma}}|^n + HB \right) \frac{1 - e^{-Pa|\hat{\boldsymbol{\gamma}}|}}{|\hat{\boldsymbol{\gamma}}|}, \quad (23c)$$

where we have introduced the dimensionless groups

$$Re = \frac{\rho \mathcal{U}^2}{2^{\frac{n-1}{2}} \mu \left(\frac{\mathcal{U}}{\mathcal{L}}\right)^n}, \quad HB = \frac{\tau_0}{2^{\frac{n+1}{2}} \mu \left(\frac{\mathcal{U}}{\mathcal{L}}\right)^n}, \quad Pa = \frac{\mathcal{U}}{\varepsilon \mathcal{L}}. \quad (24)$$

The Reynolds number Re is the ratio of inertial forces to (power-law) viscous ones, while the Herschel-Bulkley number HB quantifies the effect of yield stress versus power-law viscosity. The Papanastasiou number Pa measures the degree of regularisation employed in the apparent viscosity, with higher Pa being a more accurate description of unregularised viscoplasticity. It is worth noting that the Reynolds number for Newtonian flow ($n = 1$) is $Re_N = \rho \mathcal{U} \mathcal{L} / \mu$. When we have information about the dimensionless apparent viscosity η throughout our domain at a given time, we can compute a local Reynolds number field $Re_L = Re/\eta(\mathbf{x}, t)$. Finally, we introduce the Bingham number $Bi = \tau_0 \mathcal{L} / \sqrt{2} \mu \mathcal{U}$, to allow comparisons with articles written on simulation of Bingham fluids. In the remainder of this section, we use $\mathcal{L} = 1$ m, $\rho = 1$ kg/m³, $\mathcal{U} = 1$ m/s and $Pa = 400$. The cavity is discretised spatially with 256 cells in each dimension. The lid-driven cavity flow is then uniquely defined by the choices of μ , n and τ_0 . To the authors' best knowledge, reference results for Herschel-Bulkley fluids have not been presented in the literature. There are, however, plenty of results for power-law fluids and Bingham plastics. Since these two characterise separate components of the Herschel-Bulkley model, we expect that validating each of them individually is a good test for our code. Evaluation of the full Herschel-Bulkley model, based on this validation, is given in section 5.

Power-law fluids have zero yield stress, and are different from the Newtonian case when the flow behaviour index is different from unity. They were studied using a least squares finite elements formulation by Bell and Surana in 1994^[37], who presented results with $n = 1/2$ and $n = 3/2$. A third-order finite volume method with upwinding was then used to study the same problem by Neofytou in 2005^[38]. The classical way to compare results from

the lid-driven cavity test case is to drive the system to steady state, and then look at the velocity profiles in each direction at slices perpendicular to the flow. This ensures that we can compare with results from codes that can only calculate steady-state solutions.

Figure 3 shows our results for power-law fluid velocity profiles, and includes reference results from the aforementioned papers. Additionally, we include the Newtonian case with comparisons from the classical paper by Ghia et al.^[39]. It is evident that decreasing n results in less lid-induced kinetic energy propagating further down in the domain, whereas increasing it has the opposite effect. Our results align very well with those found in the literature, especially those due to Neofytou, which have the highest accuracy. We have also included the velocity profile for $n = 0.1$, in order to illustrate the transition to a viscoplastic in the limit $n \rightarrow 0$.

We recall that Bingham fluids have $n = 1$ and non-zero yield stress τ_0 . Due to the importance of accurately capturing viscoplastic behaviour, we have performed extra validation tests for this model. Figure 4 depicts velocity profiles at various Bingham numbers, with comparison to the works of Neofytou^[38] and Chai et al.^[40]. In the latter reference, a multiple-relaxation-time lattice Boltzmann model was employed to simulate non-Newtonian fluids. We see that increasing the yield-stress has an effect on the velocity profiles similar to that of lowering n for the power-law fluids, although the Bingham fluids have sharper transitions in the profile (especially noteworthy in the x -velocity). Our results are in excellent agreement with the relevant references, and we have also extended the range of Bingham numbers beyond those for which velocity profiles are available in the literature.

The second method we use for validation is locating the position of the main vortex centre within the cavity, at steady-state. A comprehensive study exploring this dependency was performed in 2014 by Syrakos et al.^[18]. We have performed simulations to steady-state for a large number of configurations of Re and Bi , and the resulting vortex locations are depicted in figure 5, alongside the results of Syrakos et al. We reiterate what they found in their paper: increasing the Bingham number moves the vortex upwards and to the right, while increasing the Reynolds number moves the vortex first towards the right, and then downwards and left to the centre. Our results agree very well with the reference results for the range of (Re, Bi) pairs covered in that study. Additionally, we have covered many more large Bingham numbers, obtaining results which follow the patterns to be expected. This illustrates the capability of our code to simulate fluids with very large yield stress.

The most important validation for viscoplastic fluids, is the accurate determination of yield surfaces. Regions where the stress satisfies $|\boldsymbol{\tau}| \leq \tau_0$ are known as unyielded regions. The interface which separates yielded and unyielded regions is called the yield surface. Since the yield surface separates two fundamentally different states of mat-

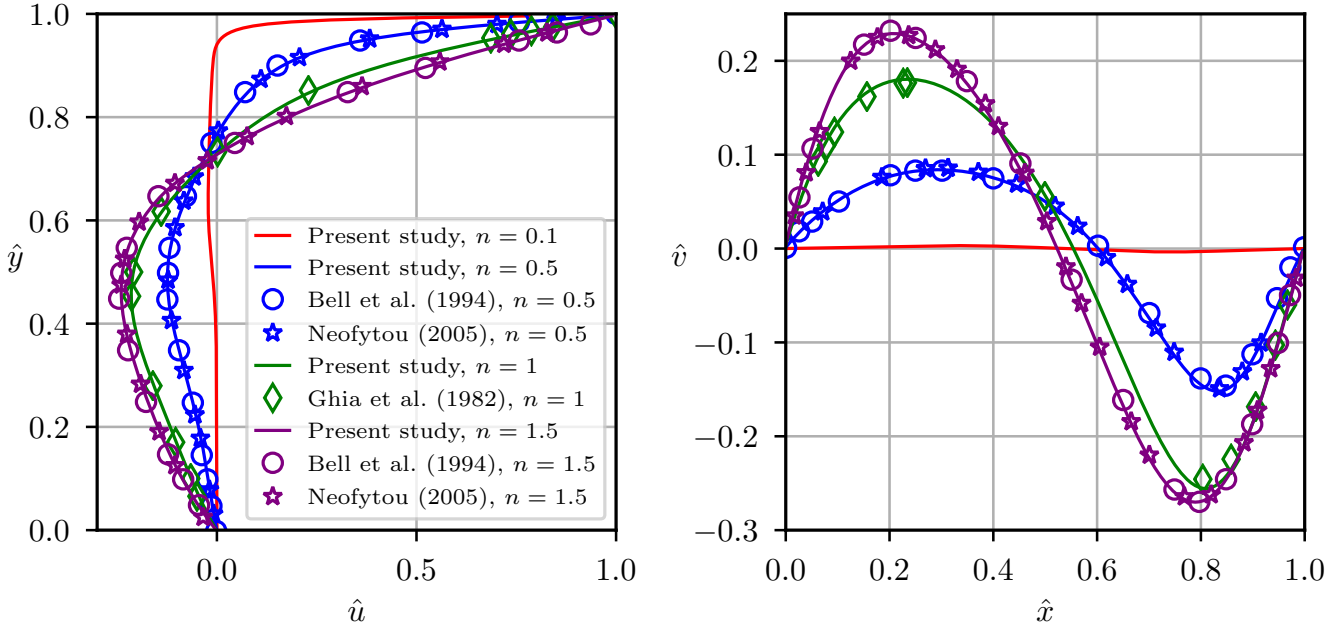


Figure 3: Velocity profiles for power-law fluids with $\mu = 0.01 \text{ Pas}^n$. Left: First component of velocity through the vertical slice $\hat{x} = 0.5$. Right: Second component of velocity through the horizontal slice $\hat{y} = 0.5$.

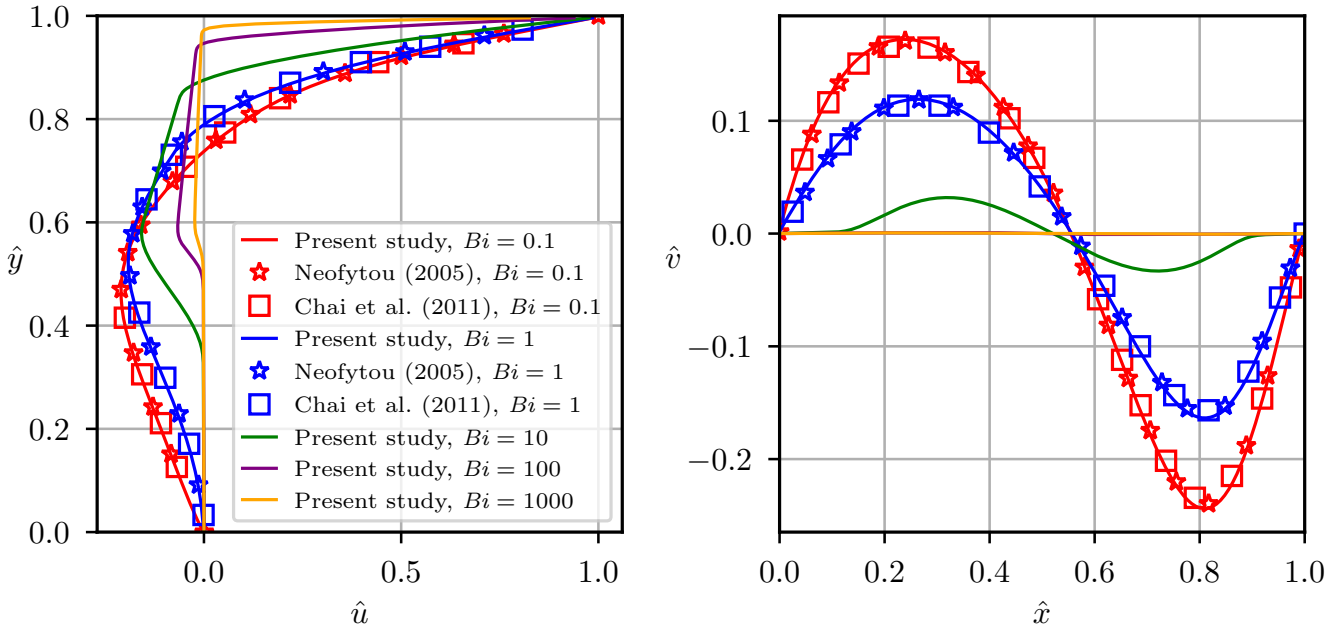


Figure 4: Velocity profiles for Bingham fluids with $Re = 100$. Left: First component of velocity through the vertical slice $\hat{x} = 0.5$. Right: Second component of velocity through the horizontal slice $\hat{y} = 0.5$.

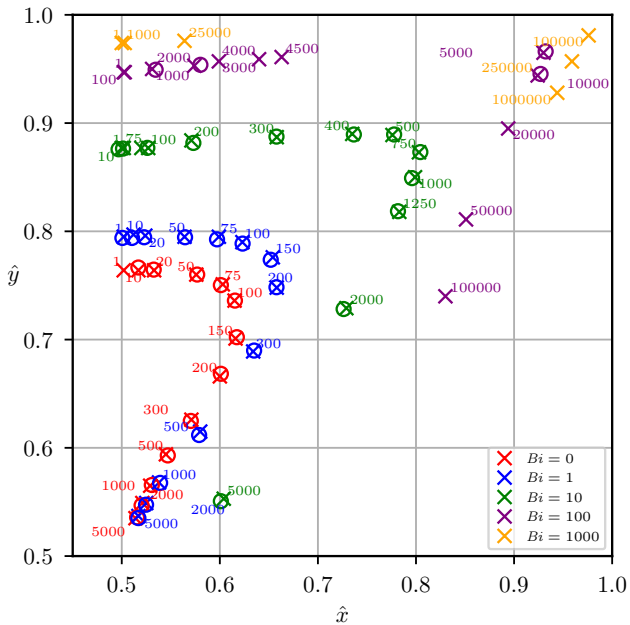


Figure 5: Vortex centre locations in the two-dimensional lid-driven cavity for Bingham fluids. Circles are results from Syrakos et al. [18], while crosses correspond to results from the present study. The number next to each point is the corresponding Reynolds number.

ter (viscous fluid flow and rigid solid behaviour), locating it precisely is a valuable metric for evaluating numerical results. Finally, we would like to ensure that our time-marching scheme accurately captures the fluid movement. In order to validate both of these two attributes, we run a simulation starting from rest and evolving to the steady-state for the lid-driven cavity. Note that the criteria for the system having reached steady-state is that the maximum relative change in the velocity field from one iteration to the next is less than some tolerance (in our case 10^{-5}). At this point, we set the lid velocity to zero, and let the system come to rest again through cessation. When the entire domain is an unyielded region, we stop the simulation. Although some authors have used time-stepping schemes to advance the system to steady-state [41,42], we are not aware of any results illustrating the yield surface development for instantaneous start from rest. On the other hand, the latter half of this numerical experiment, i.e. cessation of Bingham fluids from the lid-driven steady-state, was studied numerically by Syrakos et al. in 2016 [19]. Comparisons with their yield surfaces and time measurements therefore serve as validation for our code.

Results with $Re = 1$ and $Bi = 10$ are depicted in figure 6. The yield surface is illustrated as the single black contour line $|\boldsymbol{\tau}| = \tau_0^3$, while the heat map shows the local Reynolds number Re_L . Note that the scaling of the

³This simple method for determining the yield surface can be improved upon for regularised constitutive equations, see e.g. the work of Liu, Muller and Denn [43]

heat map is logarithmic (see top of figure 6). The first five plots (a)-(e) show the transition from rest to steady-state. It is clear that the fluid yields immediately at a very thin layer near the lid, since a large strain is applied here at $\hat{t} = 0$. Much more significant, however, are the yielded regions which quickly propagate from the top corners and in towards the middle, eventually combining together and leaving an unyielded “plug” in the upper middle part of the cavity. This process occurs very quickly, in less than one percent of the time needed to reach steady-state. The steady-state shape of the resulting plug, and the unyielded region at the bottom of the cavity, is characteristic for the chosen pair of Reynolds and Bingham numbers. Comparisons to results by Syrakos et al. show that the steady-state yield surfaces are indistinguishable. At this point ($\hat{t} = 0.020552$), the lid is abruptly halted and held still. This removes the driving force for the flow from the system, and leads to cessation of the flow. Since cessation occurs in finite time for viscoplastic fluids, the cessation time t_c , defined as the time until the entire cavity is in the unyielded state, is an important characteristic. In order to measure t_c , we introduce a new time $\tilde{t} = t - 0.020552$. We have chosen four times during flow cessation to compare with Syrakos et al. [19] and the flow patterns are very similar to their published results. Additionally, our simulations yield $t_c = 1.2844 \cdot 10^{-3}$, which is a relative difference of less than 0.9% compared to the previously published results.

5. Evaluation

5.1. Herschel-Bulkley fluids

The results in section 4 validate our code for fluids obeying power-law and Bingham rheologies, but there are no available comparisons in the literature for Herschel-Bulkley fluids, which exhibit power-law dependencies in addition to a non-zero yield stress. Consequently, simulations were performed for a viscoplastic fluid with $\mu = 0.01 \text{ Pa s}^n$ and $\tau_0 = 0.01 \text{ Pa}$, and with the flow index n equal to 0.5 (pseudoplastic), 1.0 (Bingham) and 1.5 (dilatant). The corresponding Reynolds numbers are respectively 118.9, 100.0 and 84.1, while the Herschel-Bulkley numbers are 0.59, 0.50 and 0.42. By doing so, we check that viscoplastic effects and shear-nonlinearities can be modelled simultaneously. Figure 7 illustrates the corresponding velocity profiles after the system has reached steady-state. Comparing the plots to those in figures 3 and 4, the similarities are clear. On the other hand, it is evident that we are now dealing with a hybrid of the two. Especially in the x -component of velocity with $n = 0.5$, it is clear that the profile is influenced by the yield-stress, since the peak has moved further up in the cavity and become less rounded around the edges.

Figure 8 shows the steady-state distribution of the dimensionless apparent viscosity in the cavity for the three different flow indices. Note how increasing the flow index alters the unyielded region: in addition to shrinking, the

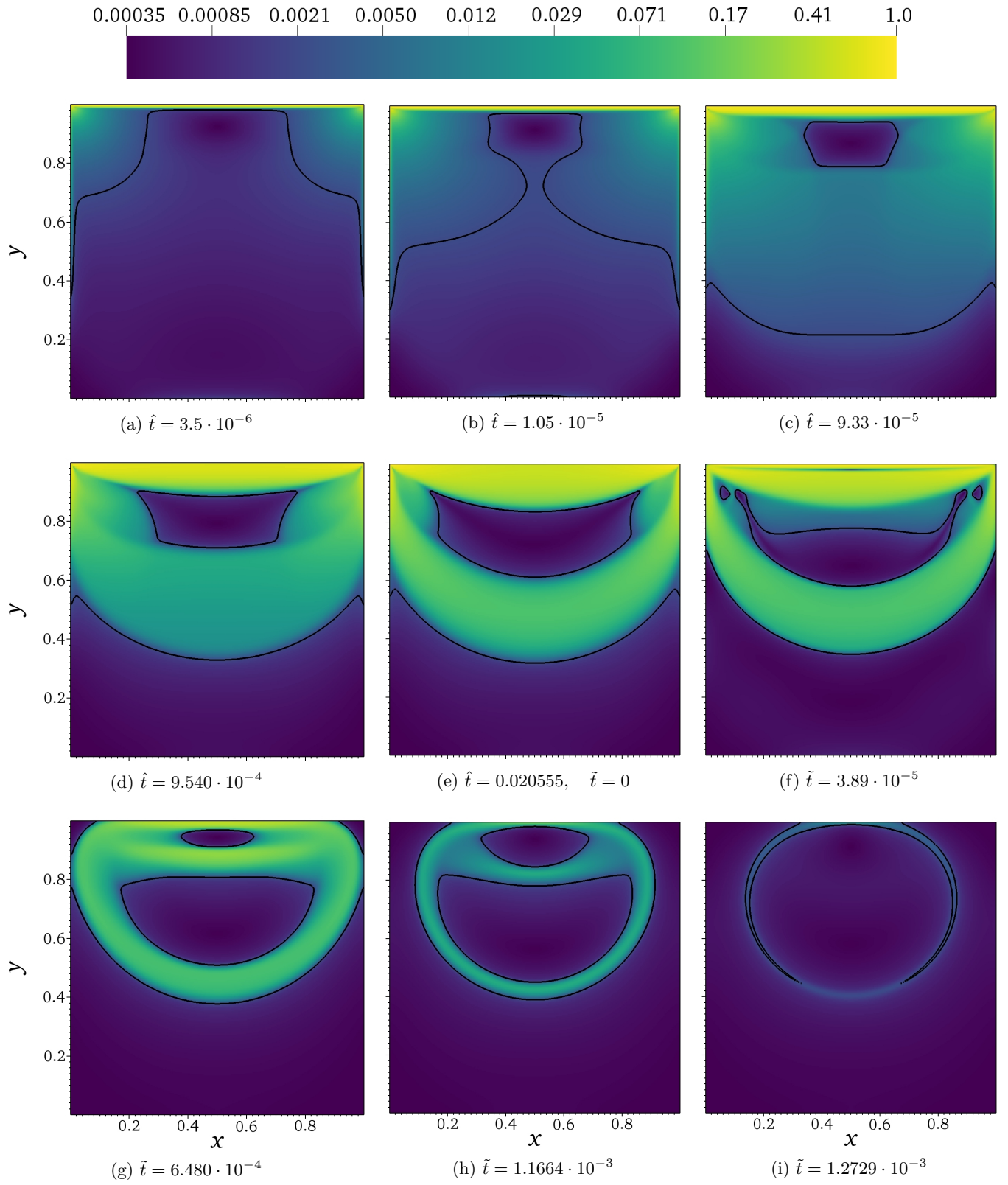


Figure 6: Yield surface and local Reynolds number for time-dependent flow in the 2D lid-driven cavity. The fluid is initially at rest, and gradually transitions to a steady state (a)-(e). At this point, the lid is stopped, allowing cessation in finite time (e)-(i).

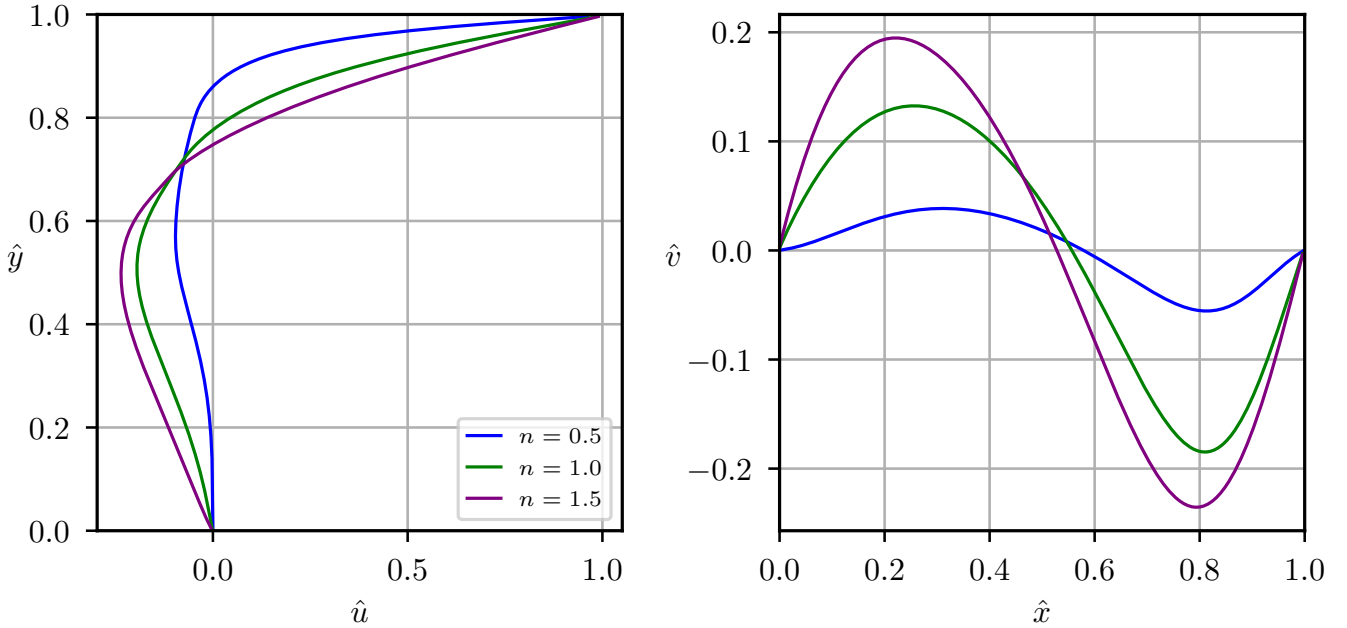


Figure 7: Velocity profiles for Herschel-Bulkley fluids with $\mu = 0.01 \text{ Pa s}^n$, $\tau = 0.01 \text{ Pa}$ and three different values of n . Left: First component of velocity through the vertical slice $\hat{x} = 0.5$. Right: Second component of velocity through the horizontal slice $\hat{y} = 0.5$.

centre plug moves towards the centre of the cavity. The fact that the smaller flow index amplifies the effect of the yield stress is as expected, since it corresponds to shear-thinning behaviour.

5.2. Moving to three dimensions

Since the augmented IAMR code is efficient and parallelises well, it is possible to run unsteady simulations of fully three-dimensional viscoplastic flows. As an extension of the lid-driven cavity for Bingham fluids in 2D, we consider a unit cube with stationary no-slip conditions on the floor and all four walls, while the lid (at $\hat{z} = 1$) drives the flow. The spatial domain is discretised using 256 cells in each directions. As before, the system is initially at rest. When steady-state is reached, we stop the motion of the lid and allow cessation to take place. Figure 9 illustrates how the yield surface evolves through time. Note that it is still computed as the contour $|\boldsymbol{\tau}| = \tau_0$, but in 3D we can actually visualise it as a surface. For a more detailed animation of the temporal evolution, please see video 1 in the supplementary material. The snapshot times in figure 9 are similar to those used in figure 6, but vary by small factors. Qualitatively, the resemblance with the 2D case is striking, as the flow clearly goes through the same steps to reach steady-state and cessation. Having said that, the third dimension allows a richer picture of the shape of the yield surface. Especially fascinating is the importance of the four vertical edges, which play a similar role as the 2D corners, and lead to the yield surface stretching out in four directions from the centre. We emphasise that this is

the first time three-dimensional yield surfaces have been presented for the lid-driven cavity case.

In figure 10, steady-state yield surfaces are shown for various combinations of Re and Bi . Readers who are familiar with the two-dimensional test case (see e.g. Syrakos et al.^[18]) will recognise the similarity between those results and slices through these three-dimensional regions. Note that the slices are taken at a slight angle in the xy -plane. These simulations illustrate the code's ability to solve the governing PDEs for time-dependent three-dimensional flows of non-Newtonian fluids following the Herschel-Bulkley model.

5.3. Parallel performance

Among the most impressive attributes of codes built within the AMReX framework, is the intrinsic scalability on state-of-the-art computer architectures. In order to demonstrate how well the parallel processing works in IAMR, we performed a weak scaling study on the supercomputer Cori. This was set up as a replication problem, where a base test is reproduced with higher and higher core counts. In the base test, a three-dimensional unit cube with periodic boundary conditions is initialised with constant density, (Newtonian) viscosity and unidirectional velocity field. Within this system, a passive scalar is advected. Its initial value equals one in a small sphere centred in the domain, and zero elsewhere. This sphere is advected for ten time steps, and the computational runtime per simulation time step is taken as the base reference. We then double the domain length (and number of cells) in each direction, leading to eight unit cubes, within

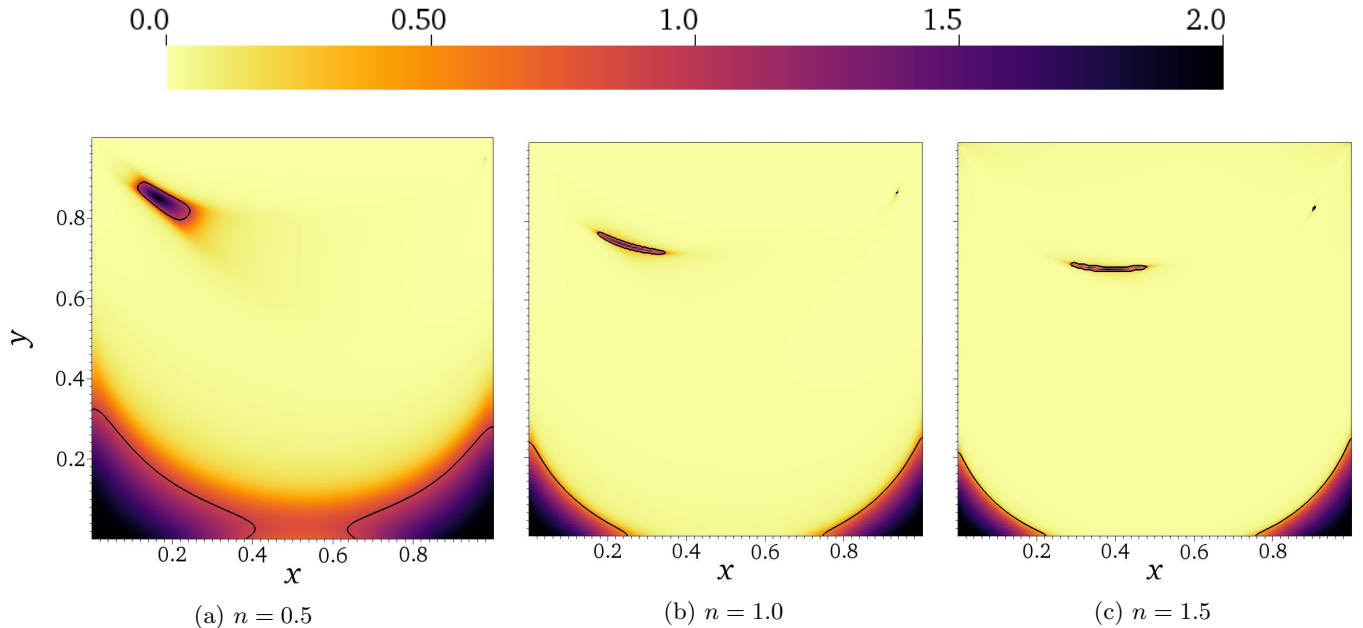


Figure 8: Viscosity distribution at steady-state for Herschel-Bulkley fluids with $\mu = 0.01 \text{ Pa s}^n$ and $\tau = 0.01 \text{ Pa}$. The black contour line marks the location of the yield surface.

Table 1: Results from replication study for weak scaling in the IAMR code. It is evident that massive parallelisation on clusters such as Cori can be utilised to simulate large problems.

Cores	Cells	Runtime
8	2,097,152	2.20 s
64	16,777,216	2.45 s
512	134,217,728	2.45 s
4096	1,073,741,824	2.80 s

each of which the same problem is set up. This ensures that the same spatial discretisation and time step size is used although the problem is much larger. Eight times as many cores are used to solve the problem, and perfect weak scaling would yield the same runtime per time step. As seen from the results in table 1, we achieve excellent performance, with only a slight increase in runtime per time step when moving from a couple of million cells to over a billion.

6. Conclusions

The publicly available software suite IAMR facilitates rapid simulations of incompressible fluids governed by the Navier-Stokes equations in a structured, adaptive framework with state-of-the-art parallelisation on contemporary supercomputer architectures. By augmenting this code, originally designed for Newtonian flows with, we allow it to deal with generalised Newtonian fluids using a regularised Herschel-Bulkley model. In doing so, we provide a code capable of simulating large-scale viscoplastic fluid systems efficiently enough to investigate three-dimensional, time-dependent systems. Thorough valida-

tion is performed through comparisons with results from peer-reviewed studies of the lid-driven cavity problem, and these benchmark results are expanded upon through a wider range of Reynolds and Bingham numbers. Finally, we have evaluated the ability of the code to deal with Herschel-Bulkley fluids, and investigated three-dimensional yield surfaces in the lid-driven cavity for the first time.

Knut Sverdrup would like to acknowledge the EPSRC Centre for Doctoral Training in Computational Methods for Materials Science for funding under grant number EP/L015552/1. Additionally, he acknowledges the funding and technical support from BP through the BP International Centre for Advanced Materials (BP-ICAM) which made this research possible.

References

- [1] S. S. Pegler, N. J. Balmforth, Locomotion over a viscoplastic film, *Journal of Fluid Mechanics* 727 (2013) 1–29.
- [2] M. W. Denny, A quantitative model for the adhesive locomotion of the terrestrial slug, *ariolimax columbianus*, *Journal of experimental Biology* 91 (1) (1981) 195–217.
- [3] A. J. Apostolidis, A. N. Beris, Modeling of the blood rheology in steady-state shear flows, *Journal of Rheology* 58 (3) (2014) 607–633.
- [4] A. J. Apostolidis, M. J. Armstrong, A. N. Beris, Modeling of human blood rheology in transient shear flows, *Journal of Rheology* 59 (1) (2015) 275–298.
- [5] A. J. Apostolidis, A. N. Beris, The effect of cholesterol and triglycerides on the steady state shear rheology of blood, *Rheologica Acta* 55 (6) (2016) 497–509.
- [6] A. J. Apostolidis, A. P. Moyer, A. N. Beris, Non-newtonian effects in simulations of coronary arterial blood flow, *Journal of Non-Newtonian Fluid Mechanics* 233 (2016) 155–165.
- [7] S. Bittleston, D. Guillot, Mud removal: research improves traditional cementing guidelines, *Oilfield Review* 3 (2) (1991) 44–54.

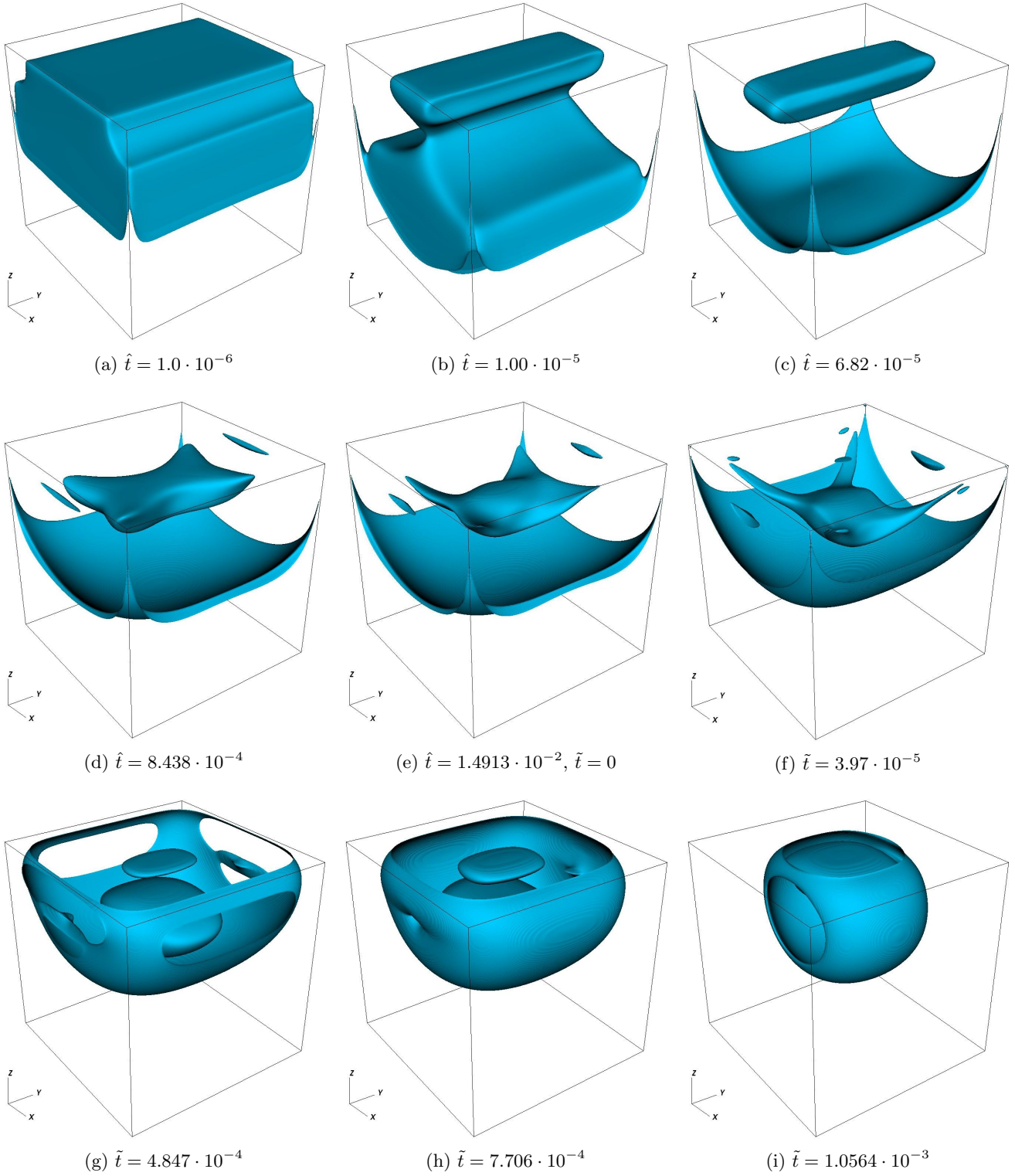


Figure 9: Three-dimensional extension of the time-dependent lid-driven cavity flow, with instantaneous start from rest evolving to steady-state. The shapes of three-dimensional plug regions of this sort have never been identified for the lid-driven cavity before.

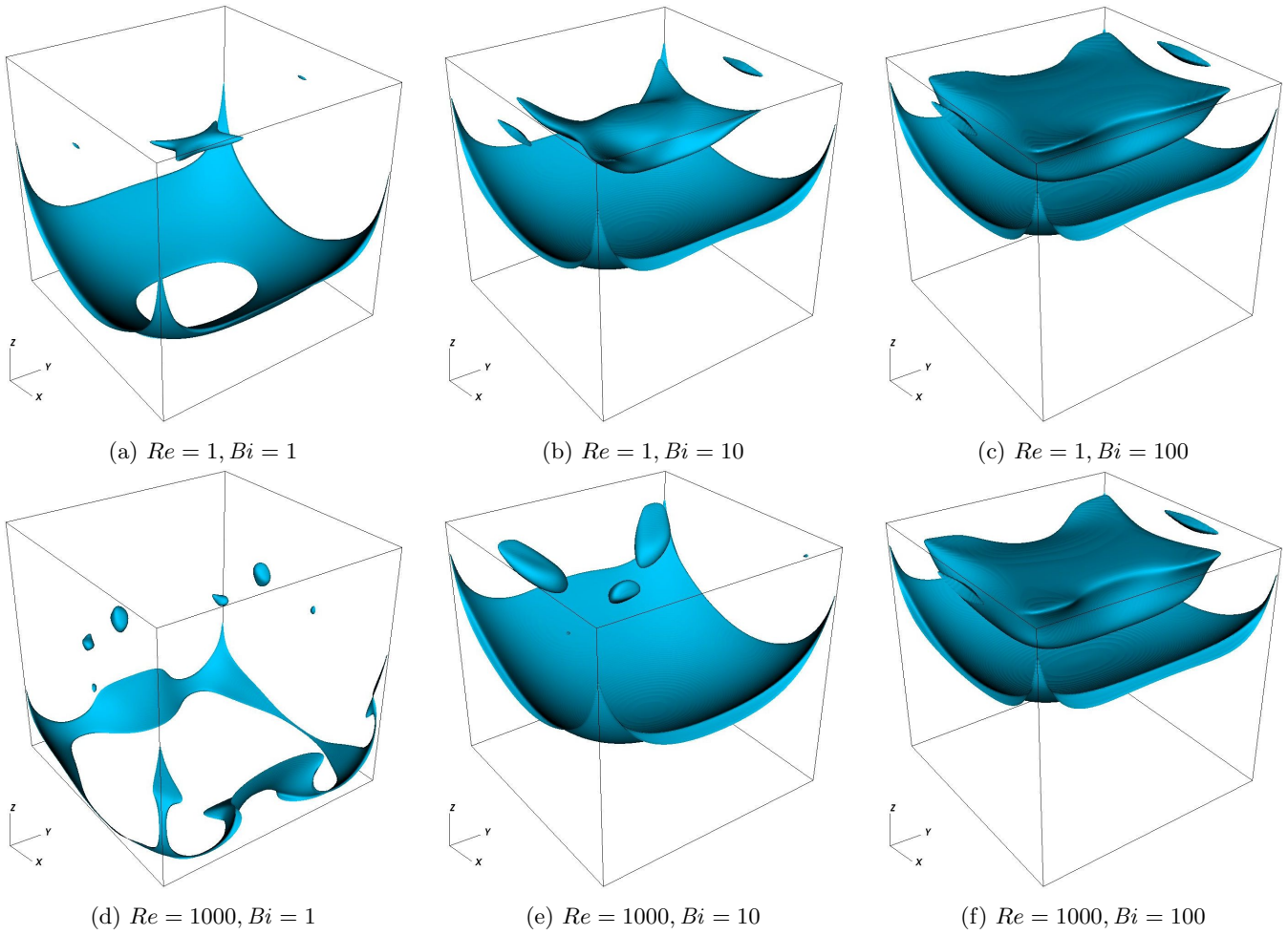


Figure 10: Steady-state yield surface for Bingham fluids with various Reynolds and Bingham numbers in the three-dimensional lid-driven cavity.

- [8] S. Taghavi, K. Alba, M. Moyers-Gonzalez, I. Frigaard, Incomplete fluid–fluid displacement of yield stress fluids in near-horizontal pipes: experiments and theory, *Journal of Non-Newtonian Fluid Mechanics* 167 (2012) 59–74.
- [9] I. A. Frigaard, K. G. Paso, P. R. de Souza Mendes, Bingham’s model in the oil and gas industry, *Rheologica Acta* 56 (3) (2017) 259–282.
- [10] M. Bercovier, M. Engelman, A finite-element method for incompressible non-Newtonian flows, *Journal of Computational Physics* 36 (3) (1980) 313–326.
- [11] R. Tanner, J. Milthorpe, Numerical simulation of the flow of fluids with yield stress, in: C. Taylor, C. Johnson, I. Smith (Eds.), *Proceedings of Third International Conference on Numerical Methods in Laminar and Turbulent Flow*, Pineridge Press, Swansea, UK, 1983, pp. 680–690.
- [12] T. C. Papanastasiou, Flows of materials with yield, *Journal of Rheology* 31 (5) (1987) 385–404.
- [13] E. Mitsoulis, T. Zisis, Flow of Bingham plastics in a lid-driven square cavity, *Journal of Non-Newtonian Fluid Mechanics* 101 (1) (2001) 173–180.
- [14] T. Zisis, E. Mitsoulis, Viscoplastic flow around a cylinder kept between parallel plates, *Journal of Non-Newtonian Fluid Mechanics* 105 (1) (2002) 1–20.
- [15] E. Mitsoulis, On creeping drag flow of a viscoplastic fluid past a circular cylinder: wall effects, *Chemical Engineering Science* 59 (4) (2004) 789–800.
- [16] E. Mitsoulis, J. Tsamopoulos, Numerical simulations of complex yield-stress fluid flows, *Rheologica Acta* 56 (3) (2017) 231–258.
- [17] A. Syrakos, G. C. Georgiou, A. N. Alexandrou, Solution of the square lid-driven cavity flow of a Bingham plastic using the finite volume method, *Journal of Non-Newtonian Fluid Mechanics* 195 (2013) 19–31.
- [18] A. Syrakos, G. C. Georgiou, A. N. Alexandrou, Performance of the finite volume method in solving regularised Bingham flows: Inertia effects in the lid-driven cavity flow, *Journal of Non-Newtonian Fluid Mechanics* 208 (2014) 88–107.
- [19] A. Syrakos, G. C. Georgiou, A. N. Alexandrou, Cessation of the lid-driven cavity flow of Newtonian and Bingham fluids, *Rheologica Acta* 55 (1) (2016) 51–66.
- [20] M. Fortin, R. Glowinski, Chapter III: On decomposition-coordination methods using an augmented Lagrangian, in: M. Fortin, R. Glowinski (Eds.), *Augmented Lagrangian Methods: Applications to the Numerical Solution of Boundary-Value Problems*, Vol. 15 of *Studies in Mathematics and Its Applications*, Elsevier, 1983, pp. 97 – 146.
- [21] G. Duvaut, J. L. Lions, *Inequalities in Mechanics and Physics*, Springer, 1976.
- [22] M. R. Hestenes, Multiplier and gradient methods, *Journal of Optimization Theory and Applications* 4 (5) (1969) 303–320.
- [23] P. Saramito, N. Roquet, An adaptive finite element method for viscoplastic fluid flows in pipes, *Computer Methods in Applied Mechanics and Engineering* 190 (40) (2001) 5391–5412.
- [24] D. Vola, L. Boscardin, J. Latché, Laminar unsteady flows of Bingham fluids: a numerical strategy and some benchmark results, *Journal of Computational Physics* 187 (2) (2003) 441–456.
- [25] T. Treskatis, M. A. Moyers-Gonzalez, C. J. Price, An accelerated dual proximal gradient method for applications in viscoplasticity, *Journal of Non-Newtonian Fluid Mechanics* 238 (2016) 115–130.
- [26] P. Saramito, A damped Newton algorithm for computing viscoplastic fluid flows, *Journal of Non-Newtonian Fluid Mechanics* 238 (2016) 6–15.
- [27] S. Enayatpour, E. van Oort, et al., Advanced modeling of cement displacement complexities, in: *SPE/IADC Drilling Conference and Exhibition*, Society of Petroleum Engineers, 2017.
- [28] A. Almgren, J. Bell, P. Colella, L. Howell, M. Welcome, A conservative adaptive projection method for the variable density incompressible Navier–Stokes equations, *Journal of Computational Physics* 142 (1998) 1–46.
- [29] H. A. Barnes, The yield stress – a review or $\pi\alpha\upsilon\tau\alpha\rho\epsilon\iota$ – everything flows?, *Journal of Non-Newtonian Fluid Mechanics* 81 (1) (1999) 133–178.
- [30] N. J. Balmforth, I. A. Frigaard, G. Ovarlez, Yielding to stress: recent developments in viscoplastic fluid mechanics, *Annual Review of Fluid Mechanics* 46 (2014) 121–146.
- [31] P. Saramito, A. Wachs, Progress in numerical simulation of yield stress fluid flows, *Rheologica Acta* 56 (3) (2017) 211–230.
- [32] E. C. Bingham, An investigation of the laws of plastic flow, *Bulletin of the Bureau of Standards* 13 (2) (1916) 309–353.
- [33] J. Oldroyd, A rational formulation of the equations of plastic flow for a Bingham solid, in: *Mathematical Proceedings of the Cambridge Philosophical Society*, Vol. 43, Cambridge University Press, 1947, pp. 100–105.
- [34] W. H. Herschel, R. Bulkeley, Konsistenzmessungen von Gummibenzollösungen, *Colloid & Polymer Science* 39 (4) (1926) 291–300.
- [35] R. B. Pember, L. H. Howell, J. B. Bell, P. Colella, W. Y. Crutchfield, W. Fiveland, J. Jessee, An adaptive projection method for unsteady, low-mach number combustion, *Combustion Science and Technology* 140 (1-6) (1998) 123–168.
- [36] M. S. Day, J. B. Bell, Numerical simulation of laminar reacting flows with complex chemistry, *Combustion Theory and Modelling* 4 (4) (2000) 535–556.
- [37] B. C. Bell, K. S. Surana, p -version least squares finite element formulation for two-dimensional, incompressible, non-Newtonian isothermal and non-isothermal fluid flow, *International Journal for Numerical Methods in Fluids* 18 (2) (1994) 127–162.
- [38] P. Neofytou, A 3rd order upwind finite volume method for generalised Newtonian fluid flows, *Advances in Engineering Software* 36 (10) (2005) 664–680.
- [39] U. Ghia, K. N. Ghia, C. Shin, High-Re solutions for incompressible flow using the Navier-Stokes equations and a multi-grid method, *Journal of Computational Physics* 48 (3) (1982) 387–411.
- [40] Z. Chai, B. Shi, Z. Guo, F. Rong, Multiple-relaxation-time lattice Boltzmann model for generalized Newtonian fluid flows, *Journal of Non-Newtonian Fluid Mechanics* 166 (5) (2011) 332–342.
- [41] E. J. Dean, R. Glowinski, G. Guidoboni, On the numerical simulation of Bingham visco-plastic flow: old and new results, *Journal of Non-Newtonian Fluid Mechanics* 142 (1-3) (2007) 36–62.
- [42] L. Muravleva, Uzawa-like methods for numerical modeling of unsteady viscoplastic Bingham medium flows, *Applied Numerical Mathematics* 93 (2015) 140–149.
- [43] B. T. Liu, S. J. Muller, M. M. Denn, Interactions of two rigid spheres translating collinearly in creeping flow in a Bingham material, *Journal of Non-Newtonian Fluid Mechanics* 113 (1) (2003) 49–67.